Responsive charge transport in wide-band-gap oxide films of nanostructured amorphous alkali-gallium-germanosilicate

*J. Remondina [a], A. Paleari *[ab], N. V. Golubev [b], E. S. Ignat'eva [b], V. N. Sigaev [b], M. Acciarri [a], S. Trabattoni [a], A. Sassella [a] and R. Lorenzi [a]*

[a]Department of Materials Science, University of Milano – Bicocca, Via R. Cozzi 55, I-20125, Milano, Italy.

E-mail: alberto.paleari@unimib.it

[b]P.D. Sarkisov International Laboratory of Glass-based Functional Materials, Mendeleev University of Chemical Technology of Russia, Miusskaya Square 9, 125190 Moscow, Russia

Abstract

The demand for new responsive materials is continuously growing in several areas as a result of approaching the physical limits of technologies, which now calls for a drastic change of strategy. Here, we report on memory responsive oxide-in-oxide nanostructured films obtained by radio-frequency sputtering of a $7.5Li_2O–2.5Na_2O–20Ga_2O_3–45GeO_2–25SiO_2$ (mol%) glass target produced by melt quenching. Atomic force microscopy and scanning electron microscopy show that as-deposited oxide layers exhibit native nanophase separation, with the occurrence of Ga-rich oxide nanostructures – about 15 nm thick and 100 nm in diameter – incorporated in oxide layers about 70 nm thick. Interestingly, despite the wide band gap (above 4 eV), the nanostructured oxide films reveal the formation of unconventional electric field dependent charge transport paths across the material. The frequency and temperature dependence of electric conductivity and dielectric function highlights

n-type conduction sustained by charge percolation through the oxide layer. Importantly, the results demonstrate the occurrence of conductivity changes by more than an order of magnitude in a few volts, and trapped charge values up to 10^{16} electrons per cm^3.

Introduction

The need for a novel class of semiconductor materials for low power memory cells and, more generally, for a change of strategy in the design of microelectronic and computing systems, is continuously growing.[1] In these fields, the main requirements include low working power and responsive conduction features, particularly in the perspective of neuromorphic computing architectures and electrically induced resistive switches.[2–4] Both properties are important for the development of an energetically sustainable and efficient technology with a substantial improvement over the current state of the art. In this context, a promising approach is based on resistance change or capacitance change materials, *i.e.* systems with unconventional charge transport and/or charge accumulation properties. In such systems, the resistive and charging response to an electric solicitation is modified by the electric field itself or even by the previous responses of the system.[1] Ionic and nanostructure versions of this kind of material include dielectric systems that undergo electric field induced formation of structural nano-architectures that enable charge transport mechanisms across the material.[1,5]

Organic–inorganic materials belonging to such a class of systems incorporate chargeable nanostructures embedded in the organic matrix at a concentration suitable to activate internal charge–discharge dynamics resulting in memory effects.[5] Other studies are instead based on inorganic systems, mainly fast ion chalcogenide electrolytes and oxide ion conductors.[1] Such systems generally include metal dopants, particularly Cu and Ag species.[1,4] The ionic mobility of metal species in amorphous oxide structures allows conductive filaments to form across the dielectric matrix as a result of an applied electric field and reduction–oxidation reactions. The mechanisms involved in these processes give rise to electrically driven low- and high-resistance states, configuring ON and OFF states.

Beyond metal-based inorganic and hybrid dielectrics, unconventional responsive dielectrics can be designed by means of fully inorganic systems. Formation of conductive filaments can in fact occur in good inorganic dielectrics too, specifically when the material undergoes soft breakdown processes, as modelled in SiO_2, the paradigmatic insulating oxide of microelectronics.[6,7] Oxide-in-oxide nano-structured films might represent interesting systems in this perspective. In these materials, even though nanoparticles and the surrounding matrix are both nominally dielectric at the macroscopic scale, the composite structure at the nanoscale can promote charge transport and accumulation mechanisms. Electrically driven functions in oxide-in-oxide structures were indeed demonstrated in silica-based nanostructured

films where SnO_2/SnO nanoparticles enabled both electric and capacitance responses, as well as electroluminescence.[8,9]

In the present work, we have faced the task of investigating whether systems consisting of Ga-oxide containing silicate glasses could give rise to nanosized layered systems providing us with new strategies for obtaining electrically driven responsive materials. The idea is to take advantage of the propensity of Ga-containing silicates to generate segregated nanophases and of the concomitant potential of Ga oxide as a carrier of functional properties in the field of conductive oxides. In these Ga-containing mixed oxides, in fact, the Ga-oxide component has the potential of providing easy-to-fabricate glass-based planar systems with the peculiar optical and electrical properties of Ga-oxide nanophases,[10–15] including light-emitting features demonstrated during the past few years in nanostructured bulk glasses.[16–22] However, the detailed analysis of Ga oxide nanophases in mixed oxides has been mainly studied in bulk glass, where nanophases nucleate and grow by thermally controlled phase separation.[23–25] Instead, no data are available on analogous oxide-in-oxide compositions in planar geometry with nanosized thickness. Here, we give an answer on the nano-morphology of these types of systems and on the resulting electrical response properties. Specifically, we report on the unconventional electrical features of nanostructured Ga-containing oxide-in-oxide thin films in which the nanostructure size and thickness become comparable and cause an electric field dependent conductive and capacitance response.

Materials and methods

The rationale of the present work is summarized at a glance in Fig. 1, comprising material synthesis and thin film deposition (Fig. 1a), structural characterization and modelling (Fig. 1b, on the left), dielectric response and charge transport measurements and mechanism analysis (Fig. 1b, on the right), so as to finally give a coherent interpretation of the response.

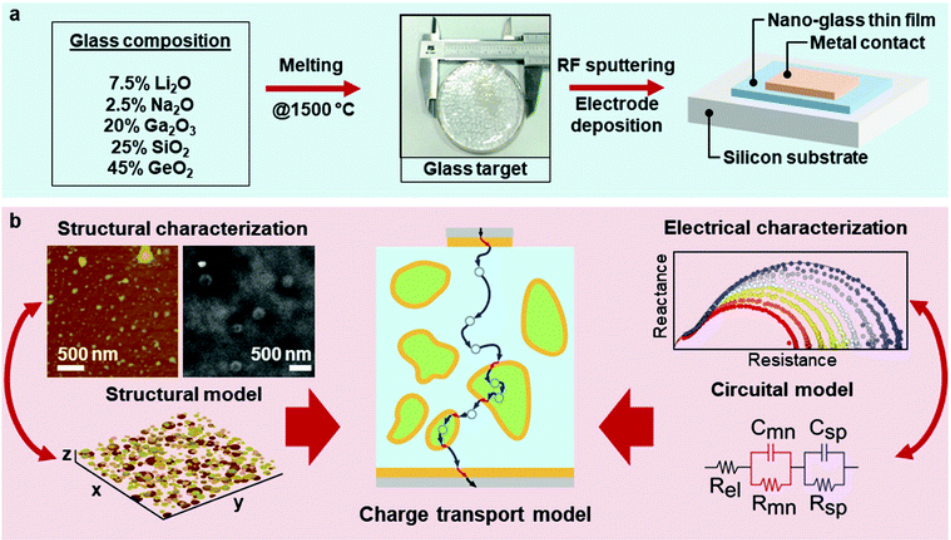

Fig. 1 *Rationale of the investigation. (a) Images of the main results of the production of nanostructured material by the melt quenching technique and consequent film deposition by RF beam sputtering. (b) Main typologies of experimental results – comprising structural (left) and electrical (right) data – and modelling of nanostructures and dielectric response data, finally resulting in the central interpretation of the charge transport mechanism.*

Glass target and film fabrication

We prepared disks of bulk glass – with the right size to be used as targets in the process of sputtering deposition of thin films – by the melt casting method, 6 cm in size and 5 mm in thickness, with a nominal composition of $7.5Li_2O–2.5Na_2O–20Ga_2O_3–45GeO_2–25SiO_2$ (mol%). As raw materials, we used amorphous SiO_2 (special purity grade), GeO_2 (special purity), Li_2CO_3 (reagent grade), Na_2CO_3 (reagent grade), and Ga_2O_3 (reagent grade). The starting materials were weighed using an analytical balance with an accuracy of 0.001 g and carefully mixed in an agate mortar. Glass was then prepared in air at 1500 °C for 60 min.

Films were deposited at a rate of about 2–3 nm min^{-1}, either on a silica substrate (for optical measurements) or silicon wafer (for complex impedance spectroscopy), *via* RF-sputtering. Final film thickness was 70 ± 5 nm. A gold electrode of about 0.5 cm^2 was then deposited by evaporation on film samples for electrical measurements, with the silicon substrate as the second electrode.

Morphological and structural characterization

Nano-morphology and compositional nanostructuring of the fabricated films were analysed by means of SEM and AFM. Electron microscopy data were collected using a Zeiss Gemini system equipped with a Bruker Quantax EDX system. AFM analysis was carried out by means of a Nanoscope V Multimode AFM Bruker instrument in intermittent contact mode, in air, with silicon tips at a resonance frequency of about 340 kHz, spring constant of 40 N m^{-1}, and tip radius of 8 nm. Film thickness was

estimated from the results of AFM analysis of step-wise reference samples and from data collected using a Veeco Dektak 8 microprofilometer.

Data on the optical functions in the spectral region from 200 to 1000 nm were collected by means of a Varian Cary 50 spectrophotometer with a spectral resolution of about 1 nm. Data on refractive index *n*, attenuation coefficient *k*, and film thickness were obtained through spectroscopic ellipsometry (SE) measurements of films on a Si substrate in the spectral range of 300–1000 nm, using a Woollam instrument. Data were collected at 65°, 70°, and 75° of incidence with a retarder plate in the optical path, with a focused beam of about 100 µm in diameter so as to limit the effects of film inhomogeneity. Regression of the data was performed using the WVASE32 software.

Electric response measurements

We collected AC data using a HP4284A LCR-meter in the frequency range between 100 Hz and 1 MHz (or between 1 kHz and 1 MHz in the case of large noise) with a modulation amplitude of 100 mV, after checking the absence of relevant changes by changing the amplitude around that value.

The effects of electric stress were analysed by applying an additional DC field over the AC modulation, using the same instrument. We applied a bias from 0 to 30 V. Data collection was carried out by an automated procedure through a custom software controlling frequency sweeping and bias ramp.

Measurements at different temperatures in the range of 77–350 K were carried out by means of an Oxford instrument Microstat-He with four electrical contacts, using liquid nitrogen as a cryogenic liquid and an automated temperature controller operating with a heating system at constant cryogenic liquid flow. Temperature variation was obtained by setting step-by-step different temperatures with an error of about 1 K and an uncertainty on the absolute value of about 10 K.

DC data were collected thanks to a custom set-up consisting of an HP E3632A DC electrical generator for voltage supply and a Keithley 199 digital multimeter for current detection, with an automated procedure of *I*–*V* data collection.

Data analysis and modelling

Data on nano-morphology and nanostructure size distribution were extracted from AFM measurements of the film surface by modelling the material as an ensemble of nanoparticles (NPs) with random distribution of radius and *X*, *Y* and *Z* coordinates within a cell with the top face congruent in size with the analysed area. Artificial cells were randomly generated imposing some bland constraints only, such as NPs being inside the material cell, NPs not touching each other, or NP height not larger than a fraction of the *XY* radius. The generated cells were then analysed by registering the NP number and size distribution for various generated cells and then averaging the values, and finally obtaining number density per unit area and radius distribution at the surface. Such a calculation was carried out on sections parallel to

the top surface and at arbitrary distance from the surface itself, so as to obtain values simulating the AFM information and suitable to be compared with the observed data of the native film surface or partially etched sample.

The output of the electric measurements, composed of resistance and reactance pairs of (R, X) values, was expressed, for each value of the monitored variables (frequency ω, temperature T, and static bias V), as real and imaginary parts Z' and Z'' of the impedance $Z(\omega,T,V)$ of the system. This output was then analysed in three different representations.

First, the data were used to generate diagrams of the frequency dependence of the real and imaginary parts of the dielectric function $\varepsilon(\omega)$ (DF). Such data were then fitted to analytic functions reproducing modified Debye-like models (DMs),[26] and the results were used to analyse to what extent the dielectric function $\varepsilon(\omega)$ was described by the sum of charge transport contributions and polarization response.

Additional information on the different contributions was extracted from data reported as the frequency dependence of the quality Q-factor and dissipation D-factor (QD), defined as the ratio between the imaginary and the real part of the impedance (Q-factor) or its reciprocal (D-factor).

Impedance data were reported in Cole–Cole (CC) plots.[27] In this representation, data were fitted as multiple overlapping semicircles, each ascribable to resistance and capacitance RC contributions of an equivalent circuit (EC) model reproducing

the response of the whole system from different mechanisms of charge transport (resistance contributions) and charge accumulation (capacitance contributions).[28]

The analysis of the temperature and bias dependence was carried out in all the representations, finally collecting families of DF-diagrams, CC-plots, and QD-spectra as a function of *T* and *V* values. In some cases, data are then transformed into current–voltage *I*–*V* curves or capacitance–voltage *C*–*V* curves to facilitate the comparison with literature data. In all the analysis, either in the DM-approach or EC-analysis, fittings were carried out, when applicable, starting from different starting points so as to avoid local minima.

Results and discussion

Deposition-induced film nanostructuring

The first relevant finding we have encountered is the native self-structuring of the as-deposited films. Previous studies on bulk Ga-containing oxide glasses – including the alkali-germanosilicate composition we consider here – indicate that bulk samples undergo crystallization at around 700 °C, with formation of γ-Ga_2O_3 nanocrystals dispersed in a glassy host.[24,25] Native bulk samples by melt quenching are amorphous glass, except for a smooth nano-inhomogeneity we detected by SANS analysis.[23]

The histogram and image in Fig. 2a give instead a neat view of the nanostructures we observe in the AFM analysis of the as-deposited films of the investigated

composition. The mean lateral size is about 40 nm with a size dispersion characterized by a full width at half maximum of about 12 nm. The surface morphology shows nanostructures emerging from the film surface by about 15 nm on average, much less than the lateral size. The mean diameter is of the same order of magnitude as the film thickness, which is about 70 nm. These data are consistent with a nanostructured system with either the architecture of nano-pillars across the film or made up of lenticular nanoparticles quite uniformly dispersed in the layer. The latter interpretation is the only one, however, that is also consistent with selective etching experiments. Indeed, HCl etching (10^{-4} M for 300 s at 27 °C) of the as-deposited films brings out more nanostructures per unit area and with larger lateral size by progressively removing the surrounding matrix, as registered in the AFM image in Fig. 2b. The analysis of the samples and the comparison with computed values (broken lines superimposed on the histograms in Fig. 2), according to a random model of nanostructured cells (representative examples are available in Fig. S1 and S2, ESI†), finally suggest that nanostructures are on average 70 nm in diameter and about 20 nm in thickness (see Fig. 2b). The effect of selective etching of the matrix around the nanostructures also gives information on the composition. Taking into account the high HCl-resistance of Ga-oxide,[29,30] such an observation appears indeed consistent with an at least partial segregation of gallium with formation of Ga-rich alkali-poor nanostructures: this effect can really make the surrounding alkali-germanosilicate matrix depleted of the Ga-oxide component and

significantly easier to etch. The segregation of HCl-resistant alkali-free SiO_2 or GeO_2 is instead less likely and in countertendency with the number of data on bulk materials, where Ga-oxide nano-segregates in silicate and germanate glasses.[16–25]

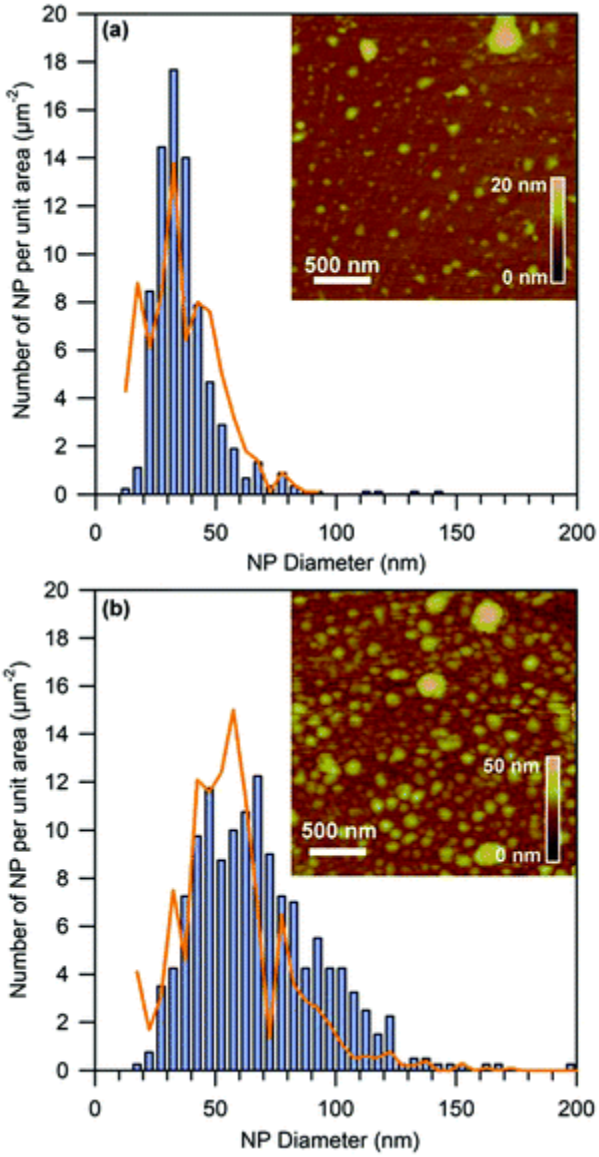

Fig. 2 Atomic force microscopy. Histograms of the number of nanostructures vs. nanostructure diameter resulting from the analysis of the film surface nano-morphology. (a) Data collected at the surface of the as-deposited film; inset: AFM image of the sampled area; continuous broken lines indicate the expected results by modelling the system. (b) The surface emerging after HCl etching. Continuous broken

lines indicate the results of a simulation modelling the film as a system of lenticular nanoparticles with given size distribution and number density, sampled at planar sections at the native surface and at an internal section.

In Fig. 3, we report the results of SEM analysis. The image in Fig. 3a confirms the presence of nanostructures, whose sizes are of the same order of magnitude observed in the AFM analysis. Importantly, the EDX analysis of the film shown in Fig. 3b gives an important indication of the nature of the segregation. From the analysis, the integrated signal from gallium atoms inside the nanostructures turns out to be systematically higher than the mean value we extract from the overall surface sampling. Instead, we find lower values than the average outside the nanostructures (inset in Fig. 3b). Actually, we cannot extract quantitative data on the distribution of gallium concentration since the EDX spatial resolution is not high enough, orthogonally to the layer, to collect the signal from a focussed nanostructure only. However, the observed differences of relative concentrations between focussed nanostructures and the matrix are statistically significant and reliably highlight that the nanostructuring process during the film deposition drives to some extent the segregation of the gallium oxide component.

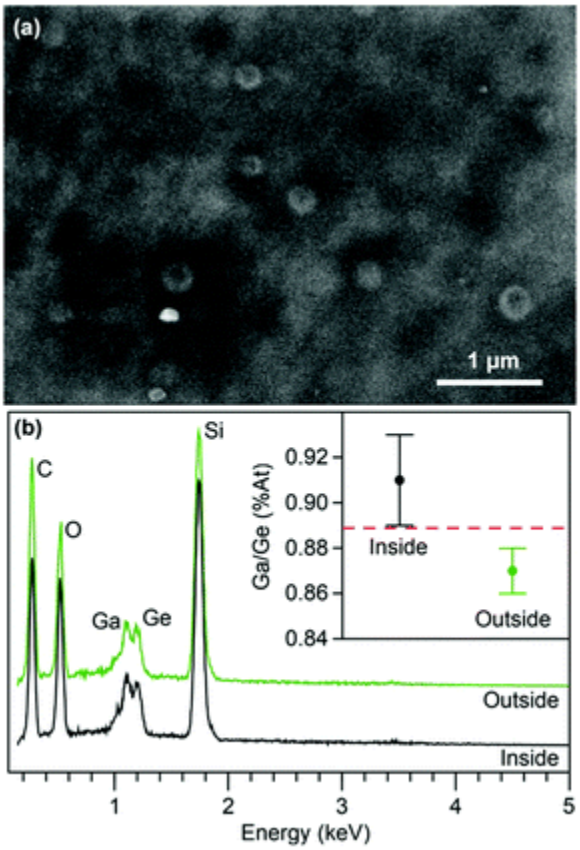

Fig. 3 *Scanning electron microscopy and energy dispersive X-ray spectroscopy. (a) SEM image of the surface of a nanostructured film. (b) Representative EDX spectra collected inside a nanostructure (bottom curve) and outside (upper curve); inset: mean value and standard error of the ratio between Ga and Ge atomic percentages as estimated by collection of EDX spectra at several points of the surface; the red dashed line indicates the nominal value expected from the glass target composition.*

Further information on the aggregation state of the whole material comes from measurements of spectroscopic ellipsometry, optical absorption, and X-ray diffraction (data are available in the ESI†): the spectral dispersion of the refractive index from ellipsometric data (Fig. S3, ESI†) matches the features expected for a

planar system with the thickness consistent with the microprofilometry value (80 ± 10 nm) and with a refractive index of 1.644 at 632 nm, consistent with the values in bulk samples.[31] This result is not obvious at all, and indeed clarifies that the deposition process gives rise to a compact layer with density and composition matching that of the glass target. Analogously, the spectral dependence of the optical absorption observed in films deposited on a transparent substrate (Fig. S4, ESI†) points to a wide-band-gap material similar to the parent glass, with an absorption edge above 4 eV and a UV shoulder at about 3.6 eV ascribable to deep levels of gallium–oxygen vacancy pairs.[32]

Despite the evidence of high reliability of the transfer process from the glass target to the film – both in composition and density – the native nanostructuring of the film represents an important difference with respect to the bulk glass and poses the question of whether such a segregation is accompanied by nanocrystallization. XRD analysis of films of this system clarifies that the observed nanostructures are not single domain nanocrystals. The pattern registers a broad structure (Fig. S5, ESI†), with a halo centred at about 24° from the germanosilicate matrix and only a broad tail at larger degrees where the main reflections from gallium oxide are expected.[25,33] The pattern resembles a basically amorphous system, in which crystalline domains, if any, are much smaller than the nanostructures observed in AFM and SEM analysis. Therefore, XRD analysis rules out the attribution of the observed nanostructures to single domain Ga_2O_3 nanocrystals. The outcome can

however be consistent with the formation of Ga-rich nanostructures – as suggested by the EDX analysis – either as Ga-rich nanostructures of amorphous mixed oxides, or as polycrystalline nanostructures with very small crystalline domains. Even pure Ga-oxide nanophases are indeed known to have a propensity to admit disorder, mainly thanks to some degree of freedom in the occupation of tetrahedral and octahedral Ga sites in the spinel structure and to variation in the oxygen stoichiometry.[11,34]

Multiple contributions to the electric response

We can discuss the functional properties of the nanostructured oxide films starting from the analysis of the dielectric response of the system under nearly non-perturbative conditions of weak oscillating stimulus (less than or equal to 100 mV) at null external stress from the DC electric field. We find a first indication about the effects of the nanostructured features in some deviation of the dielectric response from a pure Debye or distributed Debye behaviour. In Fig. 4a–c, we report representative data from our survey of frequency dependence of the dielectric response functions, collected at different temperatures from 150 K to 350 K.

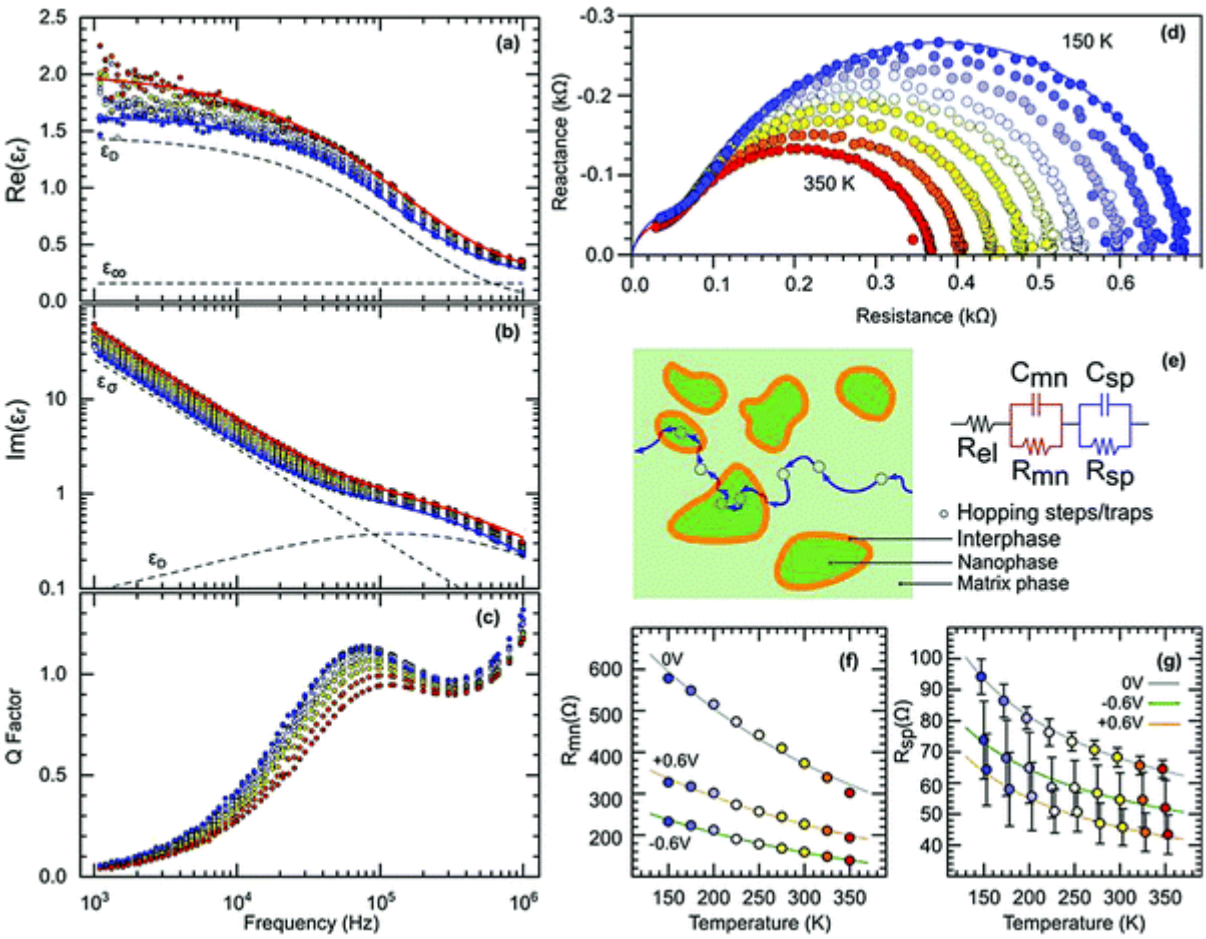

Fig. 4 Dielectric response and temperature dependence. Real (a) and imaginary (b) part of the relative dielectric function εrvs. frequency from 150 K (lower data in blue) to 350 K in a step of 25 K; results of the fit of data at two temperature values are shown by full lines as obtained by the sum of the Havriliak–Negami εD complex dielectric contribution, a purely imaginary εσ contribution of DC conduction, and a high frequency constant term ε∞ (dashed lines). Frequency dependence of the Q-factor (c). (d) Cole–Cole plots of reactance vs. resistance in the whole investigated frequency range, at different temperatures. Results of the fit at two temperatures are shown by full lines (d), according to a response model represented by an equivalent circuit (e) accounting for hopping-related conduction through a single

phase (RspCsp contribution) and barrier-limited conduction at the matrix-nanostructure interphases (RmnCmn contribution), as also depicted in the sketch, while Rel accounts for minor series contributions to the overall resistive response, mainly of extrinsic origin. Thermal dependence of the resistive components Rmn (f) and Rsp (g) at different bias; lines are fitting curves according to eqn (3) and (4), respectively.

Fig. 4a and b show the real and imaginary parts, respectively, of the dielectric function $\varepsilon(\omega)$ measured at different temperatures on a film of nanostructured glass. In the same figure, we show some examples of the fitting curves we have calculated as sum $\varepsilon(\omega) = \varepsilon_\sigma + \varepsilon_D + \varepsilon_\infty$, where ε_∞ is the high frequency value of $\varepsilon(\omega)$, while ε_σ and ε_D describe contributions from, respectively, DC conductivity σ_0

$$\varepsilon_\sigma = i\frac{\sigma_0}{\varepsilon_0\omega^s}, \qquad (1)$$

where ε_0 is the vacuum dielectric constant and s is an exponent close to unit, and from polarization mechanisms in the modified Debye approximation. In this approximation, the contribution ε_D describes a distributed mechanism of dielectric response around a characteristic resonance frequency ω_p according to the Havriliak–Negami expression[26,35]

$$\varepsilon_D(\omega) = (\varepsilon_0 - \varepsilon_\infty)\left[1 + \left(i\frac{\omega}{\omega_p}\right)^m\right]^{\frac{n-1}{m}} \qquad (2)$$

where m and n (with $m \leq 1$ and $n \geq 0$) are two parameters expressing the deviation from the purely Debye response reproduced by $m = 1$ and $n = 0$. The fit of the data registers three main facts. First, ε_σ is distinctly non-zero. This fact suggests that the material sustains a charge transport mechanism across the film clearly distinct from localized charge displacement at a specific resonance frequency related to mechanisms of polarization. Second, the polarization-related ε_D contribution fits the data for $n = 0$ and m in the range of 0.50–0.65, showing a somewhat distributed Debye response whose broadening with respect to a purely Debye system could reflect the dispersion in nanostructure (NS) size and NS-to-NS distance. Finally, even the distributed response described by $m \approx 0.5$ cannot fully reproduce the observed frequency dependence, particularly in the high frequency region. This fact is evident by plotting the data as the Q-factor – *i.e.* the ratio between the real and imaginary part of the impedance (Fig. 4c). In this representation, the results show the need for multiple contributions, registering curves with the main peak accompanied by high frequency tails caused by additional resonances from distinct mechanisms.

The opportunity to further investigate the source of such multiple contributions comes from the analysis of Cole–Cole plots in the complex impedance plane, as reported in Fig. 4d. In this representation, the data show overlapping semicircles representing contributions from concurrent mechanisms of charge transport and dielectric response by resistive and chargeable elements of an EC model. Importantly, testing the compatibility of the whole set of data with different EC

models (including nested RC contributions), we find that the resulting response is adequately reproduced by a model comprising a series circuit of two main RC elements and a minor series resistance (scheme in Fig. 4e).

This outcome provides us with a hint on the charge transport and/or charge trapping across the nanostructured film, which is responsible for the observed electric response. Nanostructured materials can in general sustain concurrent and potentially comparable mechanisms of electric conduction and polarization from different phases. The relative weight of these mechanisms in the resulting response depends on the conductivity properties of the two coexisting phases and on the potential barriers between them. In general, charge transport mechanisms comprise a number of concomitant processes, including charge transport across the matrix only, transport *via* nanoparticle-to-nanoparticle paths across the matrix and within the nanostructures, and charge transport through the potential barriers at the interfaces occurring in the system.

The observed response – pointing to an EC model composed of series elements – indicates that there is no large contribution from conduction paths involving charge transport across the matrix only, parallel with the conduction response from nanostructures and interphase barriers (in that case, a nested EC model would better fit the data). Instead, the results suggest a conduction path through sequential steps. With regards to these steps, the detection of distinct RC contributions in the Cole–Cole plots evidences the occurrence of mechanisms

characterized by quite different frequency domains or time response regimes. Accordingly, the two distinguishable contributions to the conduction process should be ascribed to qualitatively different mechanisms rather than to the compositionally different phases in the nano-structured system. In fact, barrier-limited charge transport/displacement mechanisms at the interphases between the matrix and other phases (nanostructures and electrodes) are expected to be described by a $-(R_{mn}C_{mn})-$ contribution significantly different from a barrier-free response resulting from the sum of all single-phase contributions of the wide-band-gap phases in the system. The latter single-phase response can generally be representable as a second $-(R_{sp}C_{sp})-$ circuital element, in series with the first one, according to an EC series model $-(R_{sp}C_{sp})$-$(R_{mn}C_{mn})-$ that indeed fits the data with only an additional R_{el} in series, which adjusts the response for a minor unbalanced resistance of the external electrical circuit.

Such a situation is representable as the response of a system with a matrix that behaves as a dielectric on the length scale of the film thickness, nevertheless permitting the formation of conductive pathways thanks to charge percolation from one nanostructure to the other (sketch in Fig. 4e). Interestingly, looking at the relative size of the two semicircles at low and high frequency in the data shown in Fig. 4d, we register that the less conductive process is also the process with the longer response time. Specifically, as we show below with a more detailed analysis of the temperature dependence, we can anticipate that $(R_{mn}C_{mn})$ is the main

contribution at low frequency, whereas ($R_{sp}C_{sp}$) dominates the high frequency range. In other words, $R_{mn} > R_{sp}$ with characteristic times $\tau_{mn} > \tau_{sp}$.

The data in Fig. 4d allow us to analyse in some detail the temperature dependence of the conductive response. The Cole–Cole plots register an impedance decrease with increasing temperature and point to thermally activated mechanisms of charge transport. A careful analysis also shows that the resistive contributions from R_{mn} (Fig. 4f) and R_{sp} (Fig. 4g) follow different temperature dependences. More specifically, the high frequency resistive contribution shown in Fig. 4g is well reproduced by the temperature dependence expected when charge transport processes are mediated by variable range hopping mechanisms.

Such a behaviour is encountered in disordered, but anyway homogeneous, semiconductors with localized charge states, according to Mott's law[36]

$$\sigma = \sigma_0 \exp[-(T_0/T)^{1/4}] \qquad (3)$$

The low-frequency component in Fig. 4f instead shows a different dependence, following a law of the type

$$\sigma = \sigma_0 \exp[-T_1(T_2/T)] \qquad (4)$$

which describes processes of fluctuation-induced tunnelling across barriers with a disordered distribution of parameters, as expected in disordered nanostructured systems.[37–39] According to these results, the data suggest that the charge transport across the nanostructured film is sustained by the formation of chains of conductive steps that proceed by hopping in each phase – with a response ($R_{sp}C_{sp}$) that

dominates the higher part of the frequency domain – and by tunnelling between phases, described by a response ($R_{mn}C_{mn}$) with a longer characteristic time. Additional information comes from the study under conditions of electric stress, as reported in the next section.

Static electric field effects on the material response

We report in Fig. 5 an overview of the effects of an applied electric field on the resistive and capacitive response in the investigated system. The contour plots of resistivity $\rho(V,\omega)$, relative dielectric permittivity $\varepsilon_r(V,\omega)$, and Q-factor $Q_{factor}(V,\omega)$ values in the voltage-frequency 2D-domain show that the applied field causes a relevant bias-induced decrease of resistance at low frequency (Fig. 5a) and lowers the zero-field capacity (Fig. 5b). Similar responses were reported in other studies on ceramic materials and definitely attributed to the effects of bias on the Schottky barriers at the grain boundaries.[40–43] We observe that these effects are accompanied by the parallel removal of the polarization mechanism responsible for the resonance at 10^3–10^4 Hz (Fig. 5c). This frequency region is characteristic of the electric response we have just ascribed to mechanisms involving the matrix-nanostructure barrier.

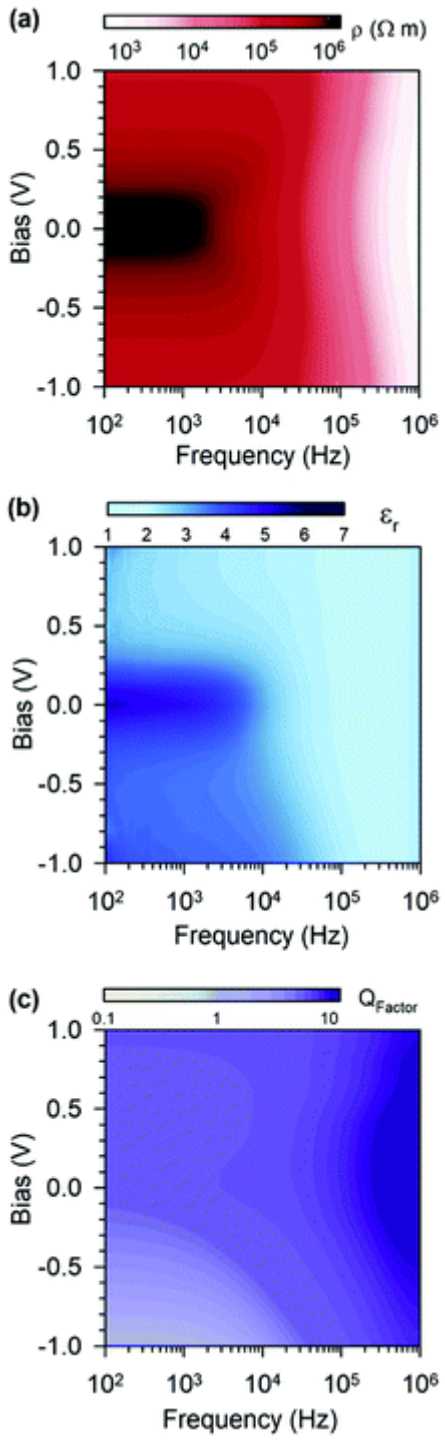

Fig. 5 Electric field effects on dielectric and charge transport response as a function of frequency. (a) Film resistivity ρ, (b) relative film permittivity εr, and (c) Q-factor of the oxide film.

We can perform a more detailed analysis of such an effect considering the complex impedance data. In Fig. 6a, we report the Cole–Cole plot of one of the investigated films undergoing electric stress at a positive applied static voltage (with the metal electrode voltage referring to the substrate). We notice that the applied bias drastically reduces the low frequency semi-circle, registering the lowering of the R_{nm} contribution. The high frequency component of the complex impedance is instead much less influenced by the static electric field. As reported in Fig. 6b and c, the dielectric response *vs.* frequency is modified by increasing voltage. Specifically, we register the enhancement of the conduction-related ε_σ contribution responsible for the linear behaviour in Im(ε) (Fig. 6c), and the decrease of the dielectric Debye-like component in Re(ε) with a resonance band in the low frequency region between 10^3–10^4 Hz (Fig. 6b). Whilst these effects are quite similar at negative applied bias, we instead register an asymmetric behaviour of the dielectric component at a higher frequency of 10^4–10^5 Hz (Fig. 6d–f).

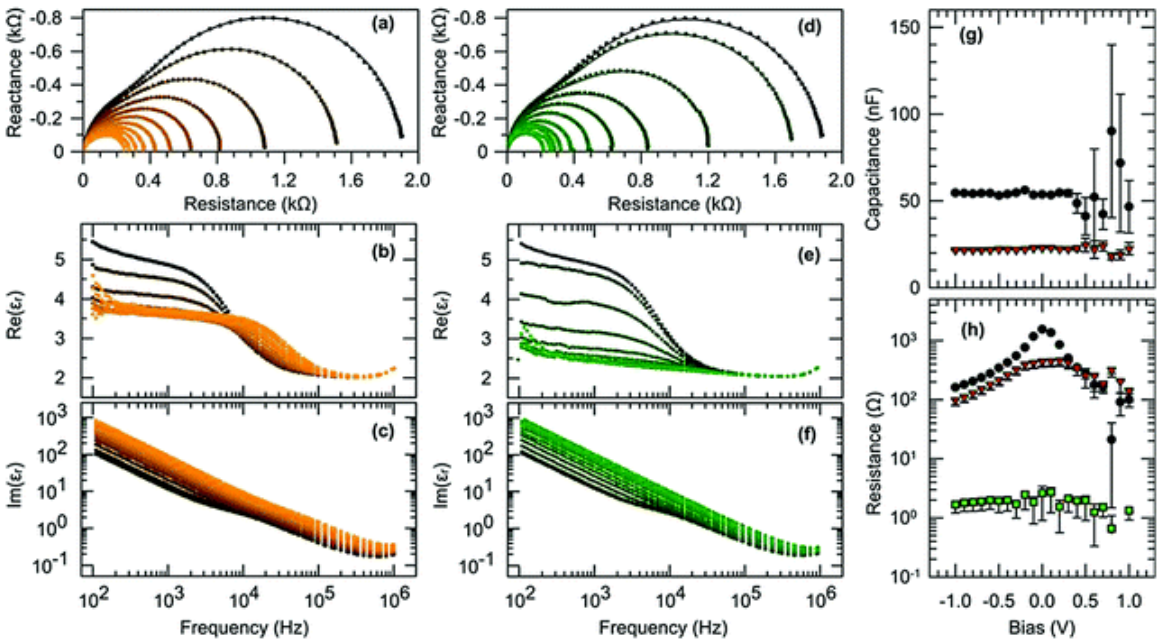

Fig. 6 Bias effects on the dielectric response. Effects of negative DC bias from 0 V (dark colour) to −1 V (light colour) in steps of 0.1 V on (a) reactance vs. resistance, and on the real (b) and imaginary (c) parts of the relative dielectric function. Effects of positive DC bias from 0 V (dark colour) to +1 V (light colour) in steps of 0.1 V on (d) reactance vs. resistance, and on the real (e) and imaginary (f) parts of the relative dielectric function. Capacitance (g) and resistance (h) values of the mn-, sp-, and el-contributions (circles, triangles, and squares, respectively) resulting from the analysis of the data within a series EC model.

This component vanishes at positive bias – parallel to the lowering of the low-frequency component – while it does not vanish and indeed slightly increases upon application of a negative bias, with a corresponding effect in the high frequency part of Im(ε). Whilst no relevant effect is registered for the capacitance contributions

(Fig. 6g), the data of R_{mn} and R_{sp} in Fig. 6h highlight that a moderate applied voltage in the range of ±1 V effectively causes a relevant change of the low frequency component of the conduction response, with a lowering of R_{mn} by an order of magnitude at 1 V. The change of the high frequency component is less pronounced, reflecting – as we anticipated above – the weaker effect of the electric field on the hopping mechanism compared with the effect on the tunnelling-limited process of conduction across the nanostructured film.

No effect is instead detected in the minor series contribution R_{el}, which, in fact, is not directly related to the intrinsic response of the material.

Charge transport in a disordered nanostructured system

The results shown in Fig. 4–6 provide us with an interesting view of the electric conduction process in the investigated system, highlighting a field-dependent response and a relevant role of the disorder. On the one hand, in fact, the results shown in Fig. 6h indicate a nonlinear electric response consisting of an activation effect of the applied electric field on the mechanisms governing the conduction process. On the other hand, the thermal activation of the conduction process registers the occurrence of disorder-related mechanisms, consisting of fluctuation-induced tunnelling and variable-range hopping (Fig. 4f, g and eqn (3), (4)). Importantly, both processes – especially tunnelling, but also hopping – can be modified by static electric fields through the perturbation of the local potential

responsible for barriers to the charge transport and for the occurrence of localized states.[41] Therefore, the electric response registered by the data in Fig. 4–6 calls for the occurrence of voltage-dependent barriers and localized states with a non-negligible distribution of their related features. Spatial fluctuations of the local potentials are expected in structurally amorphous phases. Furthermore, the occurrence of barriers with distributed effects on the electric conduction can be associated to the nanostructured features registered in the AFM and EDX analyses in Fig. 2 and 3, specifically to the observed distribution of nanostructure sizes and nanostructure inter-distances. In other words, the conduction is sustained by charge percolation through a network of conductive pathways with distributed and field-dependent conductivity values.

Charge trapping and capacitance responsivity

The distribution of nanostructure sizes and inter-distances can provide the conductive system with additional responsive functions that are related to charge trapping and consequent modification of capacitance. In fact, the presence of a distribution of field-dependent conductive pathways can generate not only charge transport across the film but also charging processes within the nanostructured material. Charge percolation across the system can cause voltage-dependent charge transport to dead-end lines of the conductive network, which possess an entry path but no exit path in the field direction to further transfer the charge to the

electrode.[8] The nonlinear response of the system can then be used to switch off the entry path too, by lowering the bias. As a result, the system can undergo a change of its charge state thanks to the disorder-induced occurrence of switchable dead-end steps in the conduction network. Dead-end lines, in fact, constitute the dendritic fraction of connected networks arising when the distribution of conductivity values among the possible conduction steps is large enough. This situation causes the coexistence of efficient conductive lines together with highly resistive ones. In our system, this condition is related to two facts: first, the conduction proceeds through thermal activation between localized states across potential barriers whose features show differences, from point to point, inside the material. Second, the dependence of the conductivity on the applied electric field makes each conduction line, and the whole network, susceptible to be modified by an external bias. As a result, charge transport in a nanostructured film occurs *via* percolation through the connected network made up of the more efficient conductive lines.

Under suitable conditions – depending on how much the system is above the percolation threshold and on the ratio between conductive and dead-end lines in the network – a fraction of the charge can be accumulated at dead ends and trapped there by removing the bias responsible for switching on the entry step of the dead-end lines.

Since the ratio between charge trapping and charge detrapping is a function of the voltage – which switches on or switches off the less conductive lines – such a process gives rise to hysteretic behaviour in the capacity *vs.* voltage dependence.

In the capacitance data shown in Fig. 7a and b, we can find the trace of such a responsive function. The reported *C*–*V* curves show the capacitance at decreasing and increasing bias values, measured by means of an alternate probe signal of 100 mV at 100 kHz (similar curves have been obtained at different frequencies from 100 Hz to 1 MHz). The data show a clear hysteretic response, which is consistent with the occurrence of a charging process. The hysteretic behaviour and the resulting charge accumulation are more evident at negative bias at the metal electrode, when the charge flux into the film is mainly driven by electrons injected from the metal. This result points to a dominant n-type conduction in the nanostructured films, which is indeed consistent with charge transport mechanisms mediated by the electron trapping sites of germanosilicate[44] matrices and by the donor levels caused by oxygen vacancies in Ga-oxide phases.[14]

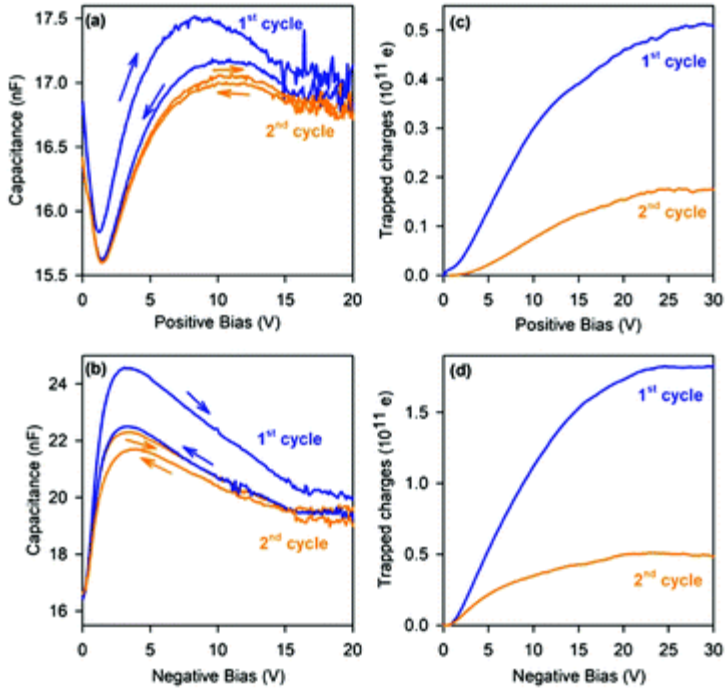

Fig. 7 Bias induced charge trapping response. Capacitance vs. bias at (a) positive and (b) negative voltage at the metal electrode. Increasing and decreasing the applied voltage, starting from initial null bias, are indicated for two repeated cycles. (c and d) Calculated trapped charge in bias cycles at positive and negative voltage, respectively.

From the capacitance data shown in Fig. 7a and b, we can calculate the number of elementary charges n (V) that turn out to be trapped at a given bias. Such trapped charges are related, in fact, to the difference of capacitance when, after increasing the bias from zero to the maximum negative value, the bias is then gradually decreased to zero along the hysteretic cycle. The resulting values n (V) = $V[C_{down}$ (V)–C_{up} (V)]/$|e|$, where C_{down} and C_{up} are the capacitance values in the two lines of the hysteresis and $|e|$ is the electron charge, are shown in Fig. 7c and d. The maximum

trapped charge corresponds to n values of the order of 10^{10}–10^{11} electrons, depending on the range of applied bias between ±3 V or ±30 V. Interestingly, the number N_{NS} of nanostructures (NSs) from the analysis of the AFM images (Fig. 2) is of the order of 10^{10} in the volume of the investigated samples (corresponding to a NS number density of the order of 10^{15} cm^{-3}). This result points to more than one electron per NS on average.

Without an independent estimation of the average charge per NS, we cannot estimate the maximum fraction of charged NSs. However, taking an electronic trap concentration δ_T of 10^{18}–10^{19} cm^{-3} – a value consistent both with the typical concentration of defects in germanosilicate glasses[45] and with the oxygen vacancy content in gallium oxide systems[46] – we can expect a maximum number n_{NS} of electrons per NS given by $n_{NS} = \delta_T V_{NS}$ taking an average NS volume V_{NS} of 10^{-15} cm^3 from the analysis and modelling of the AFM images. In such a case, n_{NS} results in approximately 10^3–10^4 trapped electrons per NS and the estimated fraction $\xi = n/(n_{NS}N_{NS})$ of chargeable NSs ranges from fractions of % to a few % of the total number of NS. Since the investigated thin films can accommodate only a few NSs along their thickness, the fraction ξ of chargeable NSs represents the approximate number of dead-end lines out of the total number of conductive lines in the system.

Furthermore, looking at Fig. 7c and d in more detail, we notice that the shape of the n (V) curve suggests more than one component, as evidenced by bumps and

slope changes. This result highlights that the dead-end lines involved in the charging process are characterized by a broad and multi-modal distribution of the bias values responsible for switching them on and off in the network. This in turn suggests that the structural features determining the barriers to the conduction process are also characterized by some multi-modal distribution. This feature appears consistent with the distribution of NS size extracted from the AFM images (Fig. 2). The broader the distribution of NS size in a nanostructured system, the wider the distribution of distances between NSs and of the properties that are dependent on the NSs themselves, including the line conductivity of the percolation network.

Conclusions

The results of the investigation allow us to point out a number of facts. First, our data show that inorganic thin films made up of an oxide-in-oxide system of wide-band-gap nanostructures in an amorphous dielectric matrix can work as a responsive material. Second, the analysis of the temperature dependence of the dielectric response demonstrates that such a responsivity can be obtained from an electric conduction based on the formation of charge percolation paths *via* at least two main concurrent mechanisms – hopping between defect sites and tunnelling through interphase Schottky barriers. Third, the investigated system exemplifies a bias-dependent response with both charge transport across the film and charge trapping in the film volume, at technologically relevant bias values of the order of a

few volts. Finally, as a fundamental result, on the basis of all previous facts, the structural analysis shows for the first time that gallium oxide amorphous alkali-germanosilicates can be transferred by RF sputtering deposition in thin planar systems that preserve composition and favour a native nanostructuring whose characteristic size is comparable with the system thickness and enables the formation of efficient conduction paths.

Acknowledgements

Financial support from the Italian Ministry of University and Research (MIUR) through grant “Dipartimenti di Eccellenza-2017 Materials for Energy” is gratefully acknowledged. The work was also supported by the Mendeleev University of Chemical Technology under Project no. 023-2018. The authors gratefully thank Arezou Azarbod and Raluca A. Mereu for their help in the film deposition procedure.

Notes and references

1 M. N. Kozicki and H. J. Barnaby, Semicond. Sci. Technol., 2016, 31, 113001.

2 S. Desbief, A. Kyndiah, D. Gue´rin, D. Gentili, M. Murgia, S. Lenfant, F. Alibart, T. Cramer, F. Biscarini and D. Vuillaume, Org. Electron., 2015, 21, 47–53.

3 L.-Q. Qi, D.-Y. Pan, J.-Q. Li, L.-H. Liu and H.-Y. Sun, Nanotechnology, 2017, 28, 115702.

4 L. Gao, Y. Li, Q. Li, Z. Song and F. Ma, Nanotechnology, 2017, 28, 215201.

5 F. Alibart, S. Pleutin, O. Bichler, C. Gamrat, T. SerranoGotarredona, B. Linares-Barranco and D. Vuillaume, Adv. Funct. Mater., 2012, 22, 609–616.

6 M. S. Munde, D. Z. Gao and A. L. Shluger, J. Phys.: Condens. Matter, 2017, 29, 245701.

7 A. Padovani, D. Gao, A. Shluger and L. Larcher, J. Appl. Phys., 2017, 121, 155101.

8 A. Paleari, S. Brovelli, R. Lorenzi, M. Giussani, A. Lauria, N. Mochenova and N. Chiodini, Adv. Funct. Mater., 2010, 20, 3511–3518.

9 S. Brovelli, N. Chiodini, R. Lorenzi, A. Lauria, M. Romagnoli and A. Paleari, Nat. Commun., 2012, 3, 690.

10 S. C. Vanithakumari and K. K. Nanda, Adv. Mater., 2009, 21, 3581–3584.

11 L. Nagarajan, R. A. De Souza, D. Samuelis, I. Valov, A. Borger, J. Janek, K.-D. Becker, P. C. Schmidt and M. Martin, Nat. Mater., 2008, 7, 391.

12 B. Fernandes, M. Hegde, P. C. Stanish, Z. L. Misˇkovic´ and P. V. Radovanovic, Chem. Phys. Lett., 2017, 684, 135–140.

13 N. Pinna, G. Garnweitner, M. Antonietti and M. Niederberger, J. Am. Chem. Soc., 2005, 127, 5608–5612.

14 M. Hegde, T. Wang, Z. L. Miskovic and P. V. Radovanovic, Appl. Phys. Lett., 2012, 100, 141903.

15 R. Lorenzi, A. Paleari, N. V. Golubev, E. S. Ignat'eva, V. N. Sigaev, M. Niederberger and A. Lauria, J. Mater. Chem. C, 2015, 3, 41–45.

16 S. Zhou, C. Li, G. Yang, G. Bi, B. Xu, Z. Hong, K. Miura, K. Hirao and J. Qiu, Adv. Funct. Mater., 2013, 23, 5436–5443.

17 S. Chenu, E. Ve´ron, C. Genevois, G. Matzen, T. Cardinal, A. Etienne, D. Massiot and M. Allix, Adv. Opt. Mater., 2014, 2, 364–372.

18 V. N. Sigaev, N. V. Golubev, E. S. Ignat'eva, A. Paleari and R. Lorenzi, Nanoscale, 2014, 6, 1763–1774.

19 S. Lotarev, A. Lipatiev, N. Golubev, E. Ignat'eva, G. Malashkevich, A. Mudryi, Y. Priseko, R. Lorenzi, A. Paleari and V. Sigaev, Opt. Lett., 2013, 38, 492–494.

20 S. V. Lotarev, A. S. Lipatiev, N. V. Golubev, E. S. Ignat'eva, L. Z. Usmanova, Y. S. Priseko, N. M. Lepekhin, A. Paleari and V. N. Sigaev, Mater. Lett., 2014, 122, 174–177.

21 V. Sigaev, N. Golubev, E. Ignat'eva, V. Savinkov, M. Campione, R. Lorenzi, F. Meinardi and A. Paleari, Nanotechnology, 2012, 23, 015708.

22 R. Lorenzi, A. Paleari, V. N. Sigaev, E. S. Ignat'eva and N. V. Golubev, Opt. Lett., 2017, 42, 2419–2422

23 V. N. Sigaev, N. V. Golubev, E. S. Ignat'eva, B. Champagnon, D. Vouagner, E. Nardou, R. Lorenzi and A. Paleari, Nanoscale, 2013, 5, 299–306.

24 N. Golubev, E. Ignat'eva, V. Sigaev, A. Lauria, L. De Trizio, A. Azarbod, A. Paleari and R. Lorenzi, Phys. Chem. Chem. Phys., 2015, 17, 5141–5150.

25 N. Golubev, E. Ignat'eva, V. Sigaev, L. De Trizio, A. Azarbod, A. Paleari and R. Lorenzi, J. Mater. Chem. C, 2015, 3, 4380–4387.

26 S. Havriliak and S. Negami, Polymer, 1967, 8, 161–210.

27 K. S. Cole and R. H. Cole, J. Chem. Phys., 1941, 9, 341–351.

28 J. R. Macdonald and W. R. Kenan, Impedance Spectroscopy: Emphasizing Solid Materials and Systems, Wiley, 1987.

29 S. Ohira and N. Arai, Phys. Status Solidi C, 2008, 5, 3116–3118.

30 S.-L. Ou, D.-S. Wuu, Y.-C. Fu, S.-P. Liu, R.-H. Horng, L. Liu and Z.-C. Feng, Mater. Chem. Phys., 2012, 133, 700–705.

31 A. Paleari, V. Sigaev, N. Golubev, E. Ignat'eva, S. Bracco, A. Comotti, A. Azarbod and R. Lorenzi, Acta Mater., 2014, 70, 19–29.

32 J. Zhang, B. Li, C. Xia, G. Pei, Q. Deng, Z. Yang, W. Xu, H. Shi, F. Wu and Y. Wu, J. Phys. Chem. Solids, 2006, 67, 2448–2451.

33 T. Wang, S. S. Farvid, M. Abulikemu and P. V. Radovanovic, J. Am. Chem. Soc., 2010, 132, 9250–9252.

34 H. Y. Playford, A. C. Hannon, M. G. Tucker, D. M. Dawson, S. E. Ashbrook, R. J. Kastiban, J. Sloan and R. I. Walton, J. Phys. Chem. C, 2014, 118, 16188–16198.

35 A. K. Jonscher, J. Phys. D: Appl. Phys., 1999, 32, R57.

36 M. Fogler, S. Teber and B. Shklovskii, Phys. Rev. B: Condens. Matter Mater. Phys., 2004, 69, 035413.

37 P. Sheng, Phys. Rev. B: Condens. Matter Mater. Phys., 1980, 21, 2180.

38 C. Filipicˇ, A. Levstik, Z. Kutnjak, P. Umek and D. Arcˇon, J. Appl. Phys., 2007, 101, 084308.

39 P. Sheng, E. Sichel and J. Gittleman, Phys. Rev. Lett., 1978, 40, 1197.

40 T. B. Adams, D. C. Sinclair and A. R. West, Phys. Rev. B: Condens. Matter Mater. Phys., 2006, 73, 094124.

41 T. Prakash, S. Ramasamy and B. Murty, AIP Adv., 2011, 1, 022107.

42 B. Yotburut, P. Thongbai, T. Yamwong and S. Maensiri, Ceram. Int., 2017, 43, 5616–5627.

43 M. Shehata and K. Abdelhady, Appl. Phys. A: Mater. Sci. Process., 2018, 124, 591.

44 G. Vaccaro, L. Panzeri, S. Paleari, M. Martini and M. Fasoli, Quat. Geochronol., 2017, 39, 99–104.

45 H. Hosono, Y. Abe, D. L. Kinser, R. A. Weeks, K. Muta and H. Kawazoe, Phys. Rev. B: Condens. Matter Mater. Phys., 1992, 46, 11445.

46 Z. Liu, X. Jing and L. Wang, J. Electrochem. Soc., 2007, 154, H440–H443.